

Research Article

Open Access



# 3D-printed magnetic-based air pressure sensor for continuous respiration monitoring and breathing rehabilitation

Nora Asyikin Zulkifli<sup>1</sup>, Wooseong Jeong<sup>2</sup>, Mijin Kim<sup>1</sup>, Cheolgi Kim<sup>1</sup>, Young Hwii Ko<sup>3</sup>, Dong Choon Hyun<sup>4,\*</sup>, Sungwon Lee<sup>1,\*</sup> 

<sup>1</sup>Department of Physics and Chemistry, Daegu Gyeongbuk Institute of Science & Technology (DGIST), Daegu 42988, Republic of Korea.

<sup>2</sup>Department of Research and Development Strategy, Korea Institute of Materials and Science (KIMS), Changwon 51508, Republic of Korea.

<sup>3</sup>Department of Urology, Yeungnam University Medical Center (YUMC), Daegu 42415, Republic of Korea.

<sup>4</sup>Department of Polymer Science and Engineering, Kyungpook National University (KNU), Daegu 41566, Republic of Korea.

\***Correspondence to:** Prof. Sungwon Lee, Department of Physics and Chemistry, Daegu Gyeongbuk Institute of Science & Technology (DGIST), 333 Techno Jungang-daero, Dalseong-gun, Daegu 42988, Republic of Korea. E-mail: swlee@dgist.ac.kr; Prof. Dong Choon Hyun, Department of Polymer Science and Engineering, Kyungpook National University (KNU), 80 Daehak-ro, Daegu 41566, Republic of Korea. E-mail: dong.hyun@knu.ac.kr

**How to cite this article:** Zulkifli NA, Jeong W, Kim M, Kim C, Ko YH, Hyun DC, Lee S. 3D-printed magnetic-based air pressure sensor for continuous respiration monitoring and breathing rehabilitation. *Soft Sci* 2024;4:20. <https://dx.doi.org/10.20517/ss.2024.11>

**Received:** 15 Mar 2024 **First Decision:** 24 Apr 2024 **Revised:** 29 Apr 2024 **Accepted:** 15 May 2024 **Published:** 24 May 2024

**Academic Editor:** Xinge YU **Copy Editor:** Pei-Yun Wang **Production Editor:** Pei-Yun Wang

## Abstract

The rapid development of point-of-care testing has made prompt diagnosis, monitoring and treatment possible for many patients suffering from chronic respiratory diseases. Currently, the biggest challenge is further optimizing testing devices to facilitate more functionalities with higher efficiency and performance, along with specificity toward patient needs. By understanding that patients with chronic respiratory diseases may have difficulty breathing within a normal range, a respiration sensor is developed focusing on sensitivities in the lower air pressure range. In contrast to the simpler airflow data, the sensor can provide respiratory air pressure as an output using a magnetic-based pressure sensor. This unconventional but highly reliable approach, combined with the rest of the simple 3D-printed design of the sensor, offers a wide range of tunability and functionalities. Due to the detachable components of the respiration sensor, the device can be easily transformed into other respiratory uses such as an inspiratory muscle training device or modified to cater for higher-ranged deep breathing. Therefore, not only does it reach very low air pressure measurement (0.1 cmH<sub>2</sub>O) for normal, tidal breathing, but the sensor can also be



© The Author(s) 2024. **Open Access** This article is licensed under a Creative Commons Attribution 4.0 International License (<https://creativecommons.org/licenses/by/4.0/>), which permits unrestricted use, sharing, adaptation, distribution and reproduction in any medium or format, for any purpose, even commercially, as long as you give appropriate credit to the original author(s) and the source, provide a link to the Creative Commons license, and indicate if changes were made.



manipulated to detect high levels of air pressure (up to 35 cmH<sub>2</sub>O for exhalation and 45 cmH<sub>2</sub>O for inhalation). With its excellent sensitivities (0.0456 mV/cmH<sub>2</sub>O for inhalation, -0.0940 mV/cmH<sub>2</sub>O for exhalation), impressive distinction between inhalation and exhalation, and fully reproducible and convenient design, we believe that this respiration sensor will pave the way for developing multimodal and multifunctional respiration sensors within the biomedical field.

**Keywords:** Chronic respiratory disease, respiration sensor, magnetic sensor, 3D-printing, tidal breathing

## INTRODUCTION

Some of the most debilitating and widespread diseases plaguing the modern world are those associated with the lungs. These diseases, usually defined as chronic respiratory diseases (CRDs), include those such as chronic obstructive pulmonary disease (COPD), asthma, occupational lung diseases, and pulmonary hypertension<sup>[1]</sup>. Typically, diagnosis of these diseases requires specialized tools such as spirometers, which can analytically quantify lung performance based on air volume and flow rate<sup>[2,3]</sup>. Beyond diagnostic purposes, however, another vital function of biomedical devices treating these diseases is to continuously monitor patient health status in their daily lives, in which a simple but robust device, such as an airflow sensor or a respiration sensor, is typically used<sup>[4]</sup>. These monitoring devices are increasingly in demand nowadays due to the rapid emergence of respiratory viruses, including the recent outbreak of the COVID-19 pandemic.

In addressing this issue, considerable effort has been devoted to developing respiration sensors with different types of sensing elements. These include more traditional choices such as using resistive<sup>[5,6]</sup>, piezoresistive<sup>[7-9]</sup>, and triboelectric materials<sup>[10,11]</sup> or through other unconventional methods such as oximeter sensors, gas sensors, humidity sensors<sup>[12-14]</sup>, forced oscillation techniques (FOT)<sup>[15]</sup>, and thermal flow sensors<sup>[16,17]</sup>. Each sensing type presents its benefits and drawbacks. While sensitivity is often a prized performance trait for sensors in general, other sensor traits such as working range, reliability, reproducibility, endurance and response time should also be considered, especially regarding the specific engineering application of the sensor. For a respiration monitoring device, the most fundamental requirement is its ability to measure the waveforms of the natural, involuntary breathing process (also called tidal breathing). To achieve this, most respiration sensors measure airflow as a common output. However, patients suffering from CRDs typically encounter obstructions in their airflow, causing them to breathe in a weaker and shallower way<sup>[18,19]</sup>. An efficient respiration sensor, therefore, should have high sensitivity within low-to-medium airflow range, provide multiple health information for easy assessment by medical professionals, and possess high reliability and reproducibility for long-term health checks and comparisons.

Magnetic sensors, which can minimize dependability on the intrinsic electrical properties of the sensing material, allow higher reproducibility and reliability than sensors based solely on conductive materials such as resistive or piezoresistive-based sensors<sup>[5-9]</sup>. These features make magnetic sensors potentially useful for their application as respiration sensors. In this study, we fabricated a simple respiration sensor modified from the concept of a magnetic-based pressure sensor developed in a previous study<sup>[20]</sup>. The sensor measured air pressure rather than airflow. While airflow measurement is a simpler and more straightforward approach, measuring air pressure output can provide more accurate and meaningful health information for medical practitioners, offering insights on not just a breathing profile but also individual ventilation and lung performance<sup>[21]</sup>. Furthermore, a combination of these abilities together with wearability and/or portability may facilitate the applicability of point-of-care sensing devices, which can allow continuous monitoring of respiratory conditions of patients and consequently lead to a faster response to any medical emergencies. However, using a magnet and a corresponding magnetic sensor is still in its

infancy within the realm of respiration sensors.

For practical and widespread use of magnetic-based respiration sensors, their fabrication methodology is crucial. Ideally, the chosen method should consider several important factors, such as ease of single and mass production, material availability and cost. While it is undeniably difficult to achieve a design that encompasses all three, additive manufacturing or three-dimensional (3D) printing offers an attractive opportunity to fulfill all requirements. In this work, we fabricated most of our sensor's external tube-shaped body using 3D printing methodology with low-cost and commercially abundant polylactic acid (PLA). Along with a magnet and a magnetic sensor, a polydimethylsiloxane (PDMS) membrane was also incorporated due to its high biocompatibility and ease of synthesis and procurement. While our tube design is not novel, our finalized prototype results in an incredibly light and small device with detachability, allowing components to be easily replaced and extra body parts to readily be added for various end purposes. One such example is the additional attachment of air hole obstructers, which will add another functionality called inspiratory muscle training (IMT) to the respiration sensor. In the practicing medical field, an IMT is commonly used to aid patients in pulmonary rehabilitation, a training exercise to guide patients into breathing normally<sup>[22-24]</sup>. When obstructions are added into the airflow, patients will have to breathe harder, allowing them to gradually strengthen the muscles involved in their breathing process. Hence, this paper showed how this extra functionality is achieved by simply changing some components of our sensor design. This also opens up a large array of possibilities for more added applications and functionality to our respiration sensor.

## EXPERIMENTAL

### Magnetic sensor fabrication and characterization

To fabricate a planar Hall magnetoresistance (PHMR) sensor, a bilayer structure comprising Ta (5 nm)/NiFe (10 nm)/IrMn (10 nm)/Ta (5 nm) was deposited on a 12 mm × 6 mm silicon wafer. A stainless steel shadow mask and a laser patterning system (KorTherm Science, Korea) were used to introduce a ring-shaped design onto the wafer. Gold electrodes were sputtered, and copper wires were attached for easy measurement. To obtain a characterization profile of the PHMR sensor, its planar Hall effect (PHE) was measured by applying an external magnetic field ( $H_{ex}$ ) via Helmholtz coil on the same plane as the current applied (1 mA, 2450 SourceMeter, Keithley, USA) and the voltage measured (2182 nanovoltmeter, Keithley, USA).

### Respiration sensor assembly

The most basic form of the respiration sensor consists of three components: the mouthpiece, the middle body (containing PDMS membrane and magnet), and the sensor body (containing PHMR sensor and airhole), which can be easily assembled and disassembled from each other [Supplementary Information 1 and Supplementary Video 1]. Detailed technical dimensions of each component can be found in Supplementary Information 2. The mouthpiece and the body holding the PHMR sensor in place were both 3D-printed (Flash Forge Adventurer 3 Pro 2, China) using PLA as material. Both components are hollow and measure 40 mm in length, but the former has an inner diameter of 16.5 mm and an outer diameter of 19 mm, while the latter has slightly smaller diameters of about 13 mm (inner diameter) and 15 mm (outer diameter). The mouthpiece component also comprises a smaller ring-shaped section (diameter = 14 mm, length = 7 mm) which can be snugly fitted into the middle body, ensuring good air seal. For the middle component, two separate parts were initially 3D-printed. One facilitates the wires from the PHMR sensor through an enclosure at its bottom, while the other holds the magnet-embedded PDMS membrane in place using a commercial adhesive (Loctite 401, USA). In the latter, to ensure continuous airflow through the whole body of the sensor, a 2 mm thick ring-shaped structure was placed in the center of the opening. A PDMS membrane was only attached on this ring section. This allows air to flow through the openings to the

sides. The 1 mm thick PDMS membrane (Sylgard 184, Dow Corning) was prepared through a drop-casting method using the 10:1 ratio of base to curing agent. Before being left to cure overnight at room temperature, a commercial neodymium (NdFeb) magnet (radius = 1.5 mm, thickness = 400  $\mu\text{m}$ ) was placed in the middle of the PDMS solution. Subsequent characterization of the PDMS sample, as described in [Supplementary Information 3](#), shows that the sample behaves well within the range of standard mechanical properties established in the literature<sup>[25,26]</sup>.

### Respiration sensor characterization and demonstration

The output voltage from the PHMR sensor was measured using a nanovoltmeter (2182 nanovoltmeter, Keithley, USA) and a continuous 1.0 mA current application (2450 SourceMeter, Keithley, USA). Measurements were monitored simultaneously on a custom-made LabView software. To characterize the respiration sensor under air pressure application, a continuous positive airway pressure (CPAP) machine (AirSense 10, ResMed, USA) was used. Air pressure provided by the machine is within the normal breathing range of a human user (5 to 20  $\text{cmH}_2\text{O}$ ).

## RESULTS AND DISCUSSIONS

The respiration sensor comprises three different parts or components, each containing an essential element in its sensing mechanism. This configuration allows physical separation and distinction between these essential elements, enabling easy removal, replacement or modification processes. For example, if the PDMS membrane becomes damaged or delaminated, one may simply remove the component holding the membrane and replace it with another one without having to touch or disassemble the rest of the sensor.

The simplified schematic in [Figure 1A](#) illustrates the three components of a sensor and its three respective essential elements: (i) the PHMR sensor component; (ii) the magnet + PDMS membrane component; and (iii) the mouthpiece. The PHMR sensor component (i) has a slightly smaller diameter than the middle magnet + PDMS membrane component (ii), allowing the former to be fitted seamlessly into the latter. Similarly, the mouthpiece component (iii) contains an extrusion with a smaller diameter, which will enable a tight fit with the magnet + PDMS membrane component (ii).

The respiration sensor is a direct-type respiration sensor that accepts and measures human breathing through inhalation and exhalation via the mouth, as demonstrated in [Figure 1B](#). While breathing through the mouth is not a natural form of breathing for most humans, it is the most efficient method for respiration measurement in clinical studies due to the inability or difficulties of some patients with CRDs to breathe normally using the nose (usually due to nasal congestion or inflammation)<sup>[27,28]</sup>.

The mouthpiece plays a rather straightforward role within the respiration sensor. During exhalation, its hollow chamber channels airflow from the mouth to the PDMS membrane, then through the four 1.5 mm wide slits on the sides which will then lead the air straight through the opening at the end of the sensor body. The reverse occurs during inhalation, whereby the low-pressure condition within the sensor chamber will cause air to flow from the outside into the mouth, similar to fluid moving through a straw.

The vital elements involved in sensing the airflow and air pressure, however, are actually the PHMR sensor and the magnet embedded within the PDMS membrane (radius = 7 mm, thickness = 1 mm), as illustrated in [Figure 1C](#). When air flows onto the PDMS membrane, its thin and flexible nature allows it to move along the airflow direction. Since the circular edge of the membrane is firmly attached on the sensor body, only the middle region of the membrane containing the embedded magnet will move. When air is no longer flowing, the viscoelastic nature of the PDMS membrane pulls it back to its original form and position.

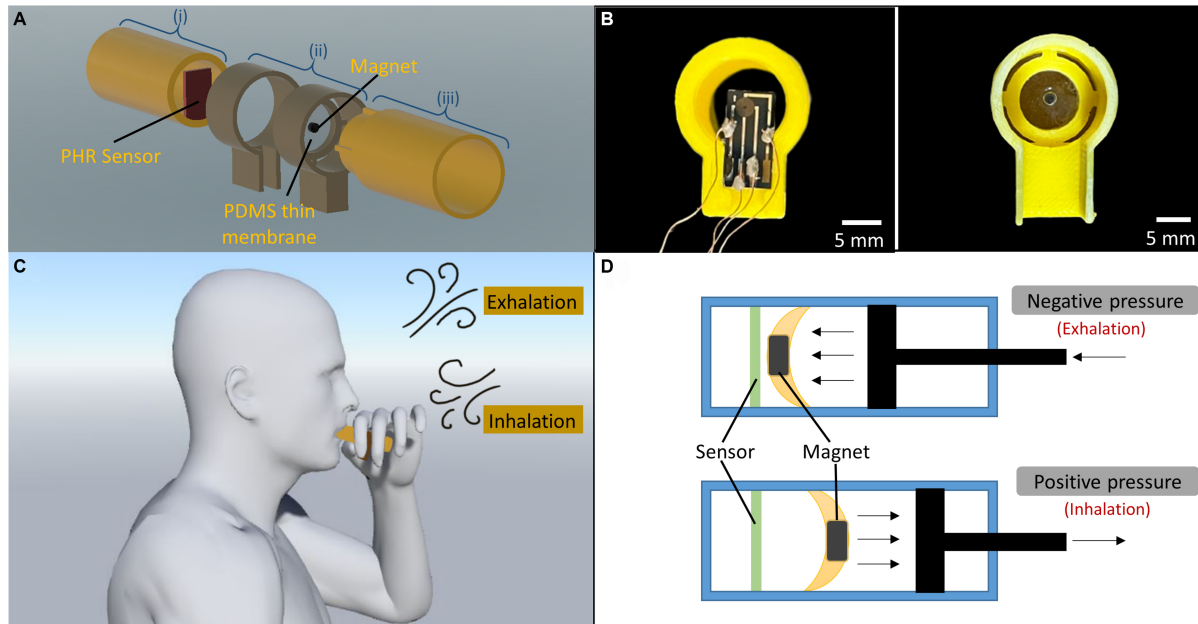


**Figure 1.** Respiration sensor design and working mechanism. (A) Full design of the respiration sensor showing parts that can be taken apart; (B) Ring-type PHMR sensor (left) and neodymium magnet embedded within a 1 mm-thick PDMS membrane (right); (C) Breathing demonstration using the respiration sensor; (D) Schematic showing the positive and negative air pressure applied on the respiration sensor. PHMR: Planar Hall magnetoresistance; PDMS: polydimethylsiloxane.

As the magnet moves according to the PDMS membrane and, thus, the airflow, the magnetic field exerted by the magnet interacts with the PHMR sensor, causing a change in the PHMR sensor's output voltage. The distance of the magnet from the PHMR sensor and the magnet's position relative to its original position determine the measured output voltage, which can then be translated into the pressure of the airflow. This pressure is bidirectional; during exhalation, the magnet moves exclusively in one direction, while in inhalation, the magnet moves in the other direction. To distinguish them, the air pressure involved in exhalation is dubbed as negative pressure, while the air pressure in inhalation is called positive pressure [Figure 1D]. This becomes the foundation of the sensing mechanism of the respiration sensor.

As the main sensing mechanism, the magnetic sensor plays a vital part in assembling the respiration sensor. In this study, a PHMR sensor was chosen, primarily due to its tendency toward a linear characterization profile, low hysteresis value, and high signal-to-noise ratio<sup>[29,30]</sup>. PHMR sensors, similar to Hall sensors, have the same current and voltage measurement directions but differ in that they measure magnetic fields on a plane. A typical Hall sensor operates in the direction in which the magnetic field is applied perpendicularly to measure the magnetic field. Several biomedical devices have also been developed in previous studies using the PHMR sensor, focusing on its robustness and reliability when compared to conventional conductive-based sensors<sup>[20,31]</sup>.

In this study, the first few experimental steps were the fabrication of the PHMR sensor, followed by characterization of its magnetic and output voltage profiles, also known as the PHE profile. An optical image of the sensor fabricated using the methodology outlined in the Experimental section is shown in Figure 2A. Figure 2B depicts a schematic of the different layers of the PHMR sensor and their thicknesses. The exchange bias coupling between the ferromagnetic (NiFe) and antiferromagnetic (IrMn) layers within the sensor produces a quantifiable output voltage ( $V_{PHE}$ ), provided that enough current source is applied. The output voltage can be expressed as follows:

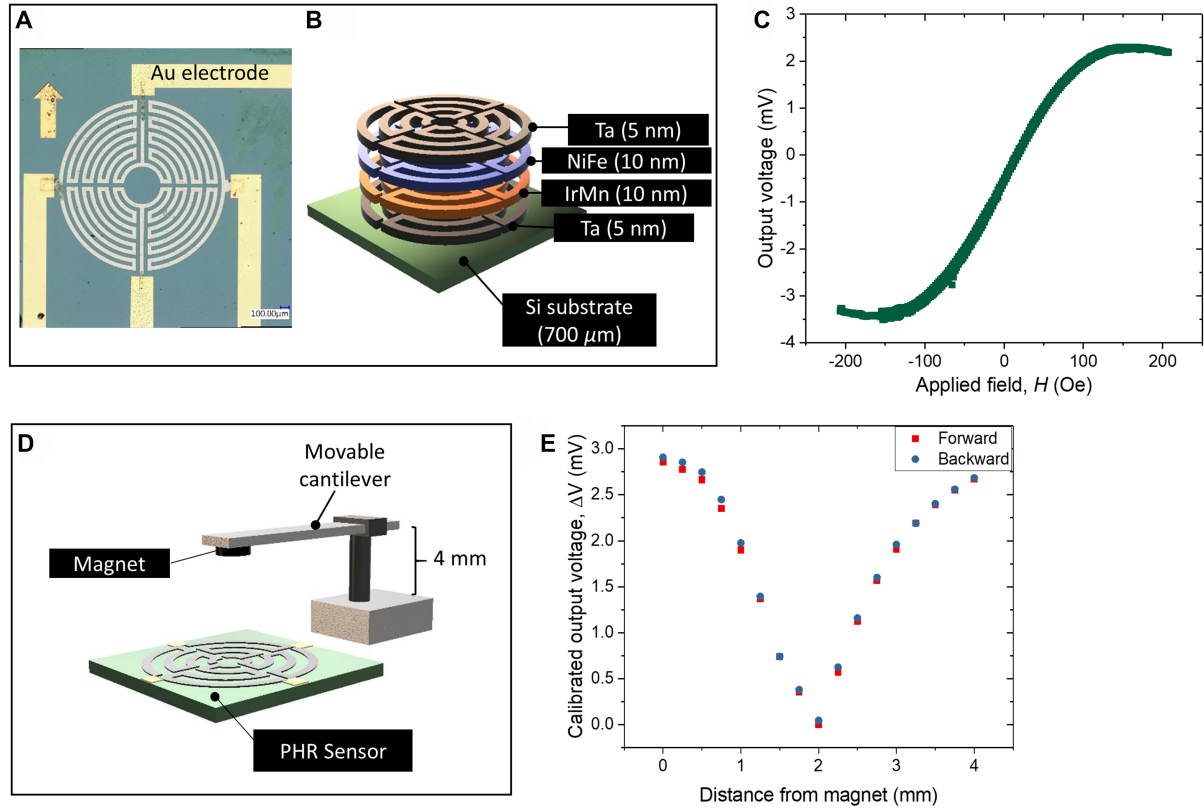


**Figure 2.** PHMR sensor's operating mechanism and PHE characterization. (A) Optical microscope image of ring-type PHMR sensor; (B) Computer-generated diagram showing the constituent layers of the PHMR sensor; (C) PHE profile of the PHMR sensor; (D) Experiment setup involved in measuring magnet-to-sensor distance; (E) Calibrated output voltage produced by PHMR sensor due to variation of magnet distance. PHMR: Planar Hall magnetoresistance; PHE: planar Hall effect.

$$V_{PHE} = \frac{I(\rho_{\parallel} - \rho_{\perp})}{t} \sin\theta \cos\theta \quad (1)$$

Where  $I$  is the active current applied,  $\rho_{\parallel}$  is the parallel resistivity,  $\rho_{\perp}$  is the perpendicular resistivity,  $t$  is the thickness of the ferromagnetic layer, and  $\theta$  is the angle between magnetization direction and the exchange bias field.

To analyze the sensor's  $V_{PHE}$  profile, the magnetization was parameterized using a Helmholtz coil [Figure 2C]. From the plot, linearity can be observed within the range of around -2.5 to 2.0 mV. Similarly, when magnetization was applied using a commercial magnet, its magnetic field strength and direction was varied by changing its distance from the PHMR sensor [Figure 2D]. A distance of 4 mm was achieved before the output voltage started to saturate and showed high nonlinearity. The result of this experiment was plotted in Figure 2E, showing its good correlation with the PHMR sensor characterization plot in Figure 2C. To further show the sensor's reliability, the comparison between forward (from 0 to 4 mm) and backward movements (from 4 to 0 mm) of the magnet are also shown in the plot. It is also important to note that the output voltage plotted in Figure 2E was calibrated to allow a more symmetrical approach to the distance variation. The calibration was performed using

$$\Delta V = V - V_0 \quad (2)$$

Where  $\Delta V$  is the calibrated output voltage,  $V$  is the instantaneous measured voltage, and  $V_0$  is the reference voltage. In this particular experiment, the  $V_0$  is the output voltage when no external magnetic field was applied. In subsequent experiments,  $V_0$  will refer to the output voltage when the magnet's distance to the PHMR sensor is at 2.0 mm. This distance was chosen due to its position as a symmetrical center point within the range shown in [Figure 2E](#).

The next set of experiments involved fully integrating the magnet and PHMR sensor into the assembled respiration sensor, as shown previously in [Figure 1A](#). In alignment with the conclusion from the previous experiment, the magnet was attached within the PDMS membrane at a distance of 2 mm from the PHMR sensor. It was also ensured to be positioned exactly within a straight line from the center of the PHMR sensor. When sensor assembly has been completed, varying levels of air pressure (both positive and negative) were applied continuously through the mouthpiece within the range of 5 to 20 cmH<sub>2</sub>O. A CPAP machine was used as an air supply due to its ability to replicate human breathing airflow during tidal breathing. However, due to the technical limitation of the machine, the lowest air pressure available was only 5 cmH<sub>2</sub>O. Our respiration sensor, however, can detect air pressure lower than that. Hence, to demonstrate a full-range air pressure characterization plot for the sensor, a polynomial (quadratic) regression curve was fitted into the measured calibrated output voltage [[Supplementary Information 4](#)]. The resulting polynomial fitted curves are depicted in [Figure 3A](#) and the fitting functions are given as follows:

Inhalation (positive pressure):

$$\Delta V = 5.235 \times 10^{-2} + 4.674 \times 10^{-2}P - 1.406 \times 10^{-4}P^2 \quad (3)$$

Exhalation (negative pressure):

$$\Delta V = 9.176 \times 10^{-3} - 0.114P + 1.582 \times 10^{-3}P^2 \quad (4)$$

Where  $\Delta V$  is calibrated output voltage in mV, and  $P$  is applied air pressure in cmH<sub>2</sub>O. The linear sensitivity for inhalation and exhalation pressure ranges are around 0.0456 mV/cmH<sub>2</sub>O and -0.0940 mV/cmH<sub>2</sub>O, respectively. Due to the nonlinearity of the exhalation curve, only the lower range shown in the shaded box (around 0 to 12 cmH<sub>2</sub>O) was considered for sensitivity calculation.

Although we already have a distance-output voltage plot in [Figure 2E](#), this experiment was conducted in a relatively unrestrained environment where the magnet and PHMR sensor were free from any static or dynamic restrictions. When integrated into the respiration sensor, however, both the magnet and PHMR sensor were attached within the sensor body. In particular, the magnet was embedded within a 1 mm thick PDMS membrane, causing its movement to become fully dependent on the structural properties of the membrane. Additionally, the instability of the PHMR sensor component itself may cause slight deformation when large air pressure was applied. These factors may lead to a slight deviation in the measured output voltage. In [Figure 3B](#), varying air pressure levels were once again plotted, but this time with respect to magnet-to-PHMR sensor distance. In particular, one dataset was plotted by comparing the output voltages in [Figure 3A](#) with the ones plotted in [Figure 2E](#), and calculating their respective air pressures. The second set of data was measured experimentally. Comparing the two data shows that while both inhalation plots agree, a slight deviation (within 3% error range) can be observed for exhalation. Since the experimental dataset represents real-life circumstances, we will proceed to use this dataset in subsequent demonstrative experiments.

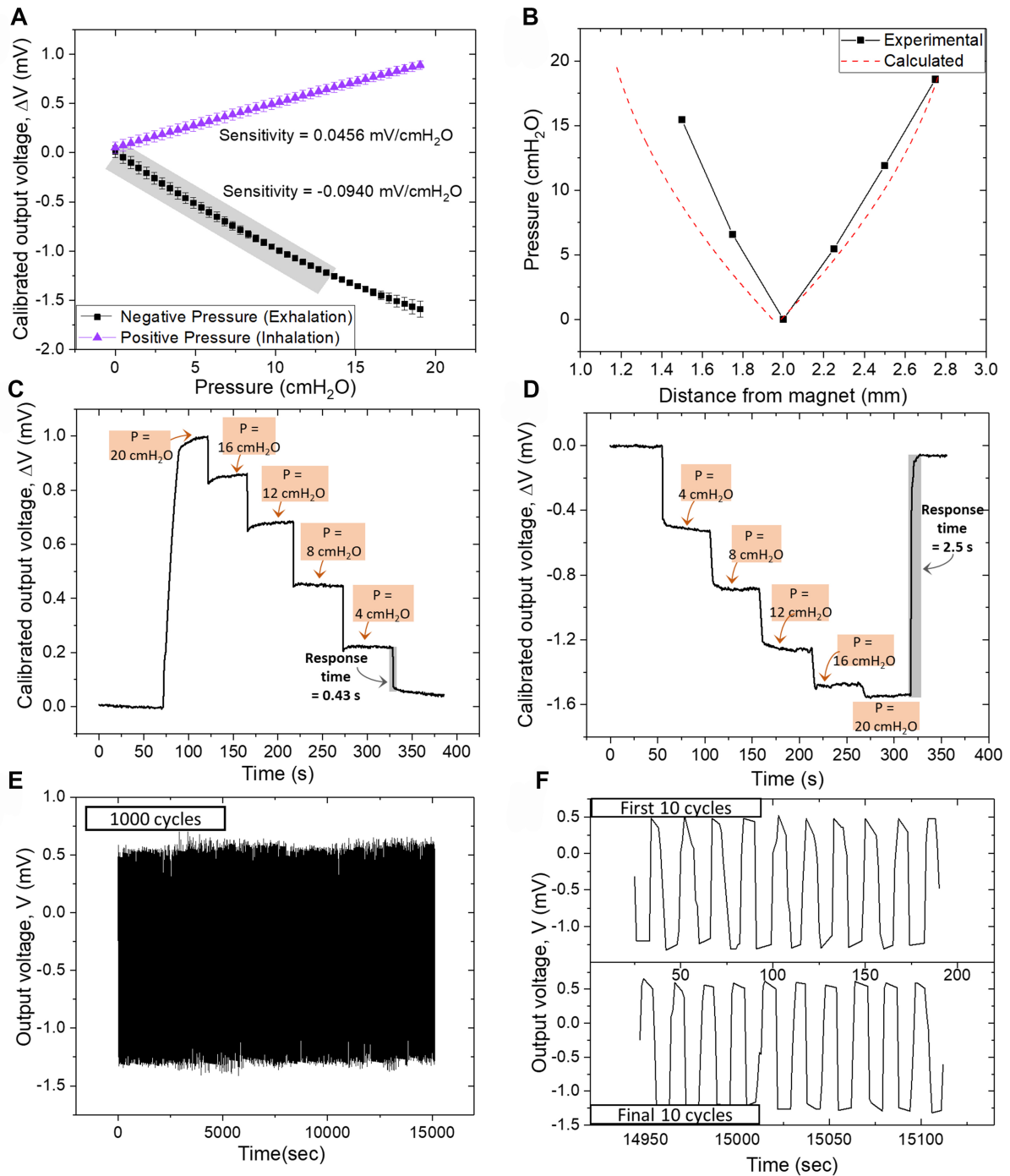


**Figure 3.** Characterization of the fully assembled respiration sensor. (A) Output voltage (calibrated) plotted against increasing air pressure (in cmH<sub>2</sub>O); (B) Correlation plot between air pressure and magnet-to-sensor distance (experimental and calculated); (C) Calibrated output voltage for step-by-step loading and unloading of positive air pressure (inhalation); (D) Calibrated output voltage for step-by-step loading and unloading of negative air pressure (exhalation); (E) Output voltage for 1,000 cycles of continuous air pressure application alternating between 8 cmH<sub>2</sub>O and -15 cmH<sub>2</sub>O; (F) The first and final ten cycles of the output voltage plot in [Figure 1E](#).

To further characterize the respiration sensor, step-by-step loading and unloading experiments were conducted for both positive and negative air pressure ([Figure 3C](#) and [D](#), respectively). The plots also show the response time for the minimum and maximum air pressure applied to the sensor. Next, to illustrate the

reliability and robustness of the sensor, a cycling test is plotted in [Figure 3E](#), whereby a positive air pressure of 8 cmH<sub>2</sub>O and a negative air pressure of 15 cmH<sub>2</sub>O were applied alternatively for 1,000 cycles. A clearer observation of the excellent reliability and output uniformity of the sensor is shown in the plots for the first and final ten seconds of the cycling plot [[Figure 3F](#)].

Next, sensor applications and demonstrations were carried out on several volunteers in a setup shown in [Supplementary Information 5](#). In [Figure 4A](#), an example of an uncalibrated, raw output voltage profile for tidal breathing of one volunteer is shown. Even without performed calibration, distinction between inhalation and exhalation remains very clear within the profile. Additionally, several other observations can be made on this plot. These are the presence of noise during idle state of the sensor, and the fluctuating breathing profile of the volunteer. Noise is a typical and unavoidable occurrence in any magnetic sensor, even those with reduced noise capabilities such as the PHMR sensor<sup>[32]</sup>. While this can be reduced by optimizing the measurement setup, providing proper shielding technique, or offsetting the measured signal in the post-processing step, this work forgoes these processes since the measurable noise is often low enough to prevent it from becoming a major deterrence to the output voltage measurement and the reliability of the sensor.

As is typical for most people, involuntary tidal breathing fluctuates frequently. Most of these fluctuations are common responses to the environment and the person's constantly changing internal body system. However, some fluctuating breathing profiles may be due to physical or emotional distress or even illnesses. This further highlights the importance of continuously monitoring respiration in the long term. However, in this work, to ensure that the major fluctuations are solely due to the fluctuating breathing pattern of human users and not the error arising from the respiration sensor, a respiration sensor validation experiment was conducted. In this experiment, the same volunteer was asked to breathe in an orderly manner, following the rhythm of a metronome with 30 beats per minute. At every beat, a sound was produced by the metronome and the volunteer had to time the start of his inhalation and exhalation at exactly the same moment as the metronome sound. The resulting plot in [Supplementary Information 6](#) shows an almost perfect intersection between the breathing pattern output and the metronome beats performed within one minute, proving the high accuracy and response time of the respiration sensor.

To show the variations between people, several volunteers demonstrated their tidal breathing using the same respiration sensor (with different mouthpieces for sanitation purposes). The resulting breathing profiles are depicted in [Figure 4B](#). Subsequently, the basic information of the volunteers and their resulting respiration rates in breaths/min (bpm) and average breathing period (time taken for one complete inhalation and exhalation cycle) are listed in [Table 1](#). All measurements fall within the air pressure range characterized for the respiration sensor. Coincidentally, a few weeks after the demonstration, one volunteer (volunteer 3) was diagnosed with COVID-19, and breathing measurement was conducted again in the second week after the diagnosis. This opportunity allows us to compare healthy (pre-COVID-19) and unhealthy (post-COVID-19) breathing profiles. Various research in recent years has provided evidence of significant changes in several breathing traits for COVID-19 patients, regardless of severity<sup>[33-35]</sup>. These include an increase in respiration rate and a decrease in breathing period. Most of these investigations, however, utilized conventional clinical devices as a form of measurement. Thus, this study proved that a similar result can be measured successfully using our fabricated respiration sensor, as illustrated in [Figure 4C](#). Although the air pressure did not show significant deviations, the respiration rate had indeed increased to a rate of 24 bpm, while the average breathing period was significantly lowered to around 2.36 s. Both these changes show good correlation to the changes reported in literature.

**Table 1. Information on the volunteers involved in the respiration sensor demonstration and application**

Volunteer	Gender	Age	Smoking	Respiration rate (bpm)	Average breathing period (s)
1	Female	30	No	11	5.32
2	Male	30	Yes	10	6.00
3	Female	22	No	19	3.06

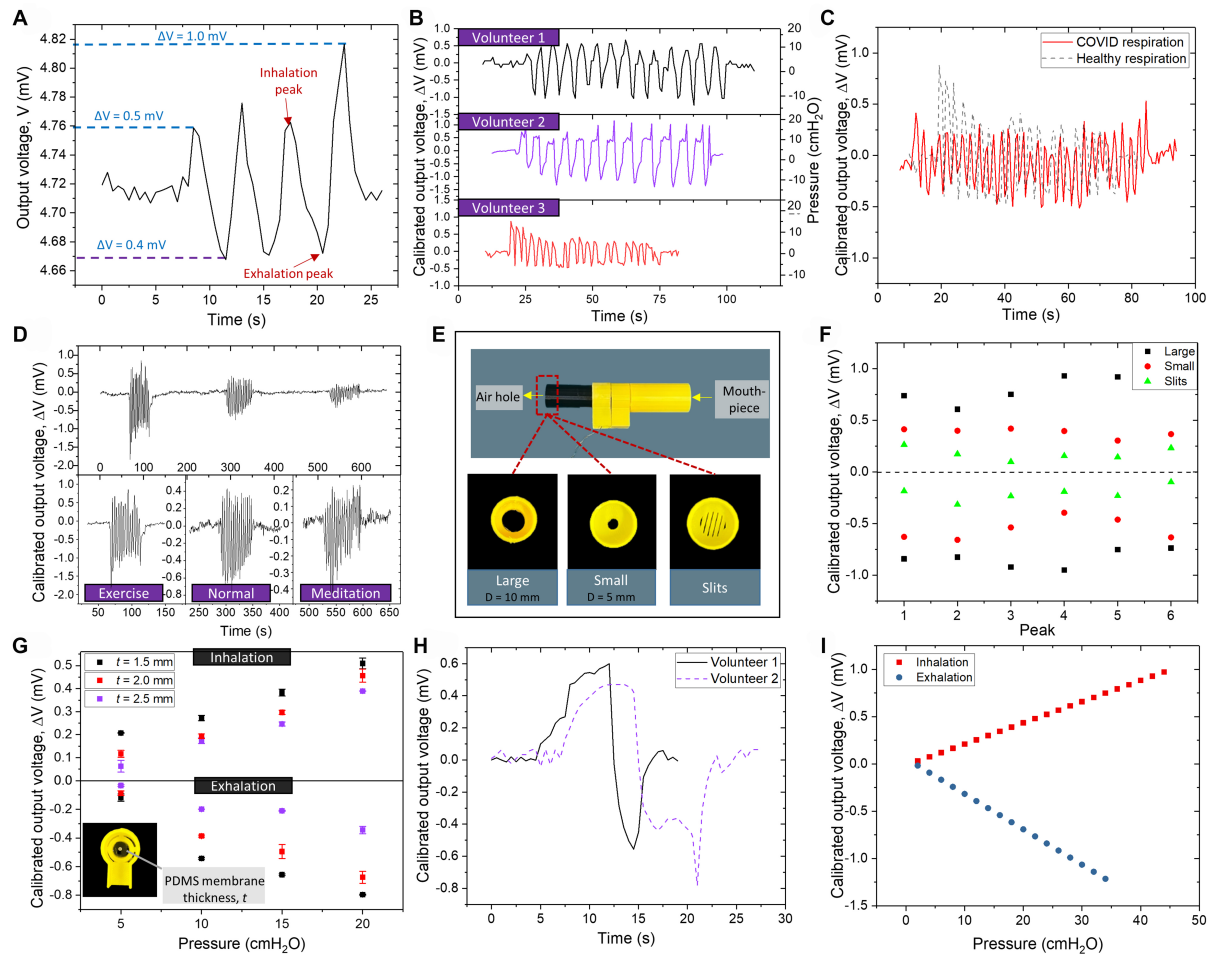


**Figure 4.** Demonstration, application and functionalization of the respiration sensor. (A) A sample data of an average individual's inhalation and exhalation pattern variation; (B) Calibrated output voltage and calculated air pressure from three volunteers' breathing profiles; (C) Breathing profiles of Volunteer 3 before and after COVID-19 diagnosis; (D) Breathing profile for normal, meditation and exercise states; (E) IMT device assembled from a modified respiration sensor with added airhole obstruction components composed of three different shapes and designs of airholes; (F) Calibrated output voltage of maximum peaks from inhalation and exhalation breathing profile of a volunteer using the IMT device; (G) Inhalation and exhalation characterization plot (calibrated output voltage plotted against increasing air pressure) for respiration sensor modified with three different thicknesses of PDMS membrane. Error bars that are not visible are smaller than the symbol size; (H) Deep breathing measurements from two volunteers using a modified respiration sensor with PDMS membrane thickness of 2.0 mm; (I) Linear regression plots (of sensors with PDMS  $t = 2.0$  mm) showing predicted output for deep breathing ranges. IMT: Inspiratory muscle training; PDMS: polydimethylsiloxane.

To further show the sensor application, one volunteer had his breathing measured in one cycle but during three different physical states: exercise, normal and meditation. The volunteer was allowed breaks from using the respiration sensor in between the three physical states to allow clearer comparison in the result. In [Figure 4D](#), the difference between the output voltages can be clearly observed, with the exercise state reaching the highest output voltage and the meditation phase being the lowest.

Due to the detachable components of the respiration sensor, it is easy for users to accommodate any extra functionalities and modifications to its uses and applications. To show such applicability, the sensor was modified to function as an IMT device by simply adding on a component at the end of the air passage that will cause obstructions towards airflow. As the name implies, an IMT device is an exercise or training tool typically used for rehabilitation of patients who have suffered from respiratory illnesses or are recovering from trauma or surgery. Athletes may also benefit from regular training of their diaphragm and lung muscles to improve their stamina and endurance<sup>[22,36,37]</sup>. The easiest method to accomplish this is to practice breathing through air resistance or obstructions. The IMT device specific for this purpose is called the passive flow resistive loading. By controlling the amount and flow of air entering and exiting the respiration sensor, we can easily replicate a similar device.

As shown in [Figure 4E](#), several components were added to the end of the respiration sensor with three distinct shapes cut into them: a large 10 mm diameter hole, a small 5 mm diameter hole, and several slits, each with a thickness of less than 1 mm. One volunteer was instructed to breathe normally through the device and the resulting output voltage profile plots were measured and recorded in [Supplementary Information 7](#). The plot in [Figure 4F](#) shows the output voltage from each peak in the inhalation and exhalation of his breathing profiles. As expected, the airflow and pressure passing through the sensor become lower as air openings get smaller. It is significantly harder to breathe with smaller allowances of air. Therefore, one of the goals of IMT is to force oneself to breathe through the device until the breathing profile reaches a certain percentage of the normal, without-IMT breathing profile (typically about 75%)<sup>[23]</sup>. Our respiration sensor, capable of continuously monitoring air pressure, is useful for this particular purpose. One can easily observe and compare their breathing patterns in different air obstructions and make appropriate changes quickly. The 3D printability of the components also gives significant ease and freedom in choosing and designing the device for IMT.

So far, the respiration sensor has shown excellent sensitivity and capability in detecting and measuring normal or tidal breathing. In particular, the device has performed remarkably well in low air pressure (0.1 cmH<sub>2</sub>O observed in [Figure 4D](#)). This is undeniably important for the main purpose of the respiration sensor, which is to cater for patients suffering from respiratory illnesses, such as COPD. Such individuals typically breathe in lower levels of airflow and air pressure, necessitating using a very sensitive, low pressure-ranged respiration sensor. However, the capability of our respiration sensor extends beyond that, allowing adaptations to accommodate higher-ranged air pressure as well. This new range allows breathing measurements that are more forceful or deeper (also called deep breathing). Information from deep breathing measurements is vital for more in-depth health diagnosis and monitoring, similar to the measurements taken with a spirometer<sup>[3]</sup>.

For the respiration sensor in this work, accommodating deep breathing can simply be done by changing the thickness of the PDMS membrane, which will inhibit the movements and deformation of the membrane when air pressure is applied. Consequently, this will cause a shorter distance traveled by the magnet, producing a lower output voltage. If we assume that the cross-sectional shape of the PDMS membrane is rectangular, we can use the equation for the second moment of area to prove the effect of thickness on its resistance to bending or deflection:

$$I = \frac{bh^3}{12} \quad (5)$$

Where  $I$  is the second moment of area, while  $b$  and  $h$  are the width and height of the rectangle, respectively. The height,  $h$ , represents the thickness of the PDMS membrane.

**Table 2. Calibrated output voltages and their respective calculated air pressures for measured inhalation and exhalation peaks from the deep breathing profiles of two volunteers**

Volunteer	Peak inhalation V (mV)	Peak inhalation P (cmH <sub>2</sub> O)	Peak exhalation V (mV)	Peak exhalation P (cmH <sub>2</sub> O)
1	0.60	27.4	-0.56	16.5
2	0.47	21.6	-0.78	22.4

Therefore, by changing the thickness of the PDMS membrane, one can easily control the range of the measured air pressure. This can be clearly observed in [Figure 4G](#), which shows the output voltages of three different thicknesses of PDMS membrane under the same air pressure application for inhalation and exhalation tidal breathing ranges. As predicted, a lower output voltage range is measured with a thicker PDMS membrane. This essentially means that the air pressure range for tidal breathing now only occupies a smaller portion of the available output voltage range. This opens up more space for a potential deep breathing air pressure range. For instance, for a PDMS membrane of thickness 2.5 mm, the highest output voltages achieved under maximum tidal breathing air pressure (20 cmH<sub>2</sub>O) is around 0.35 mV for inhalation and -0.4 mV for exhalation. This means that when compared with the linear ranges within the characterization plot in [Figure 3A](#), there are now available ranges of 0.35 to 1.0 mV (inhalation) and -0.4 to -1.2 mV (exhalation) for the measurement of deep breathing. To theoretically predict the values within these new deep breathing ranges, linear regression fits were plotted against the data for PDMS membranes 2.0 mm thick. These linear fits and their corresponding correlation equations are provided in [Supplementary Information 8](#). The resulting predicted output voltage values for possible deep breathing ranges are illustrated in [Figure 4H](#). Note that the range for exhalation only reaches a maximum pressure of 12 cmH<sub>2</sub>O due to the nonlinearity of the output voltage beyond that value, as reported previously in [Figure 3A](#). Using this predicted characterization plot, we can now determine the air pressure for deep breathing measurements conducted on two volunteers in [Figure 4I](#). The calculated values are listed in [Table 2](#).

Nevertheless, this paper will not elaborate on exploring this range but merely clarify the ability to do so with the flexible design of our respiration sensor. In future works, we aspire to further explore the wide range of potential functionality of this sensor design, such as using a spirometer or an airflow sensor.

## CONCLUSIONS

A 3D-printed respiration sensor capable of detecting and distinguishing air pressure for both inhalation and exhalation was developed using a robust magnetic PHMR sensor as its main sensing mechanism. When respiratory airflow was introduced, the magnetic field change caused by the movement of a magnet embedded within a PDMS membrane will consequently invoke a change of output voltage from the PHMR sensor. The change of the calibrated output voltage plotted against increasing air pressure can be defined by two polynomial regression curves, but some ranges with linearity can be observed and quantified. For inhalation, this includes the full range of around 0.0456 mV/cmH<sub>2</sub>O, while the lower range of exhalation has a sensitivity of -0.0940 mV/cmH<sub>2</sub>O. The sensor shows excellent step-by-step progression with a maximum response time of 2.5 s and a minimum response time of 0.43 s. Several breathing demonstrations were performed by multiple volunteers to show the diversity of breathing profiles measured by the sensor. Apart from normal breathing, demonstrations were also performed during exercise and meditation states. To accommodate the higher pressure range for deep breathing, the sensor was modified by changing the thickness of the PDMS membrane. Further modification can be easily done to expand the functionality of the sensor. To prove this, an IMT device was introduced by adding several extra components onto the sensor body. The respiration sensor design is highly adaptable and modifiable, allowing a wide range of functionalities and designs.

## DECLARATIONS

### Authors' contributions

Conceptualization, 3D-printing methodology and fabrication, data acquisition, analysis, interpretation, manuscript writing: Zulkifli NA

Conceptualization, experiment methodology, manuscript review: Jeong W

PHMR sensor fabrication, data acquisition and analysis, manuscript review: Kim M

Supervision, resources, project administration: Kim C

Conceptualization, supervision, funding acquisition, manuscript review: Lee S, Ko YH, Hyun DC

### Availability of data and materials

Data will be made available upon request.

### Financial support and sponsorship

This work was supported by the National Research Foundation of Korea (Grant Nos. 2018R1A5A1025511, 2021R1A2C1007129) and the BK21 FOUR (Fostering Outstanding Universities for Research) funded by the Ministry of Education (MOE, Korea).

### Conflict of interest

All authors declared that there are no conflicts of interest.

### Ethical approval and consent to participate

This study was conducted under the approval of the Ethics Committee of Daegu Gyeongbuk Institute of Science and Technology (DGIST) (DGISTIRB-202208-001). All participants were informed about the experimental procedure and research purposes, and have signed the relevant consent forms prior to participation.

### Consent for publication

Not applicable.

### Copyright

© The Author(s) 2024.

## REFERENCES

1. World Health Organization. Chronic respiratory diseases. Available from: <https://www.who.int/health-topics/chronic-respiratory-diseases>. [Last accessed on 22 May 2024].
2. Nepomuceno AC, Alberto N, André P, da Costa Antunes PF, de Fátima Domingues M. 3D printed spirometer for pulmonary health assessment based on fiber bragg gratings. *IEEE Sens J* 2021;21:4590-8. DOI
3. Zhou B, Baucells Costa A, Lukowicz P. Accurate spirometry with integrated barometric sensors in face-worn garments. *Sensors* 2020;20:4234. DOI PubMed PMC
4. Vanegas E, Igual R, Plaza I. Sensing systems for respiration monitoring: a technical systematic review. *Sensors* 2020;20:5446. DOI PubMed PMC
5. Al-Halhouli A, Al-Ghussain L, El Bouri S, Liu H, Zheng D. Fabrication and evaluation of a novel non-invasive stretchable and wearable respiratory rate sensor based on silver nanoparticles using inkjet printing technology. *Polymers* 2019;11:1518. DOI PubMed PMC
6. Atalay O, Kennon WR, Demirok E. Weft-knitted strain sensor for monitoring respiratory rate and its electro-mechanical modeling. *IEEE Sens J* 2015;15:110-22. DOI
7. Saha U, Kamat A, Sengupta D, Jayawardhana B, Kottapalli AGP. A low-cost lung monitoring point-of-care device based on a flexible piezoresistive flow sensor. In: 2020 IEEE SENSORS; 2020 Oct 25-28; Rotterdam, Netherlands. IEEE; 2020. p. 1-4. DOI
8. Moshizi SA, Abedi A, Pastras CJ, et al. Carbon nanofiber-reinforced Pt thin film-based airflow sensor for respiratory monitoring. *Sensor Actuat A Phys* 2022;347:113969. DOI
9. Chu M, Nguyen T, Pandey V, et al. Respiration rate and volume measurements using wearable strain sensors. *npj Digit Med* 2019;2:8. DOI PubMed PMC

10. Zhang C, Zhang L, Pu Z, Bao B, Ouyang W, Li D. Fabricating 1D stretchable fiber-shaped electronics based on inkjet printing technology for wearable applications. *Nano Energy* 2023;113:108574. DOI
11. Ghatak B, Banerjee S, Ali SB, et al. Design of a self-powered triboelectric face mask. *Nano Energy* 2021;79:105387. DOI PubMed PMC
12. Li Y, Qiu X, Xia P, et al. Enabling a low-resistance high-accuracy flowmeter for the diagnosis of chronic obstructive pulmonary disease. *Measurement* 2022;188:110551. DOI
13. De Fazio R, Stabile M, De Vittorio M, Velázquez R, Visconti P. An overview of wearable piezoresistive and inertial sensors for respiration rate monitoring. *Electronics* 2021;10:2178. DOI
14. Chen G, Guan R, Shi M, et al. A nanoforest-based humidity sensor for respiration monitoring. *Microsystems Nanoeng* 2022;8:44. DOI PubMed PMC
15. Oostveen E, MacLeod D, Lorino H, et al. The forced oscillation technique in clinical practice: methodology, recommendations and future developments. *Eur Respir J* 2003;22:1026-41. DOI PubMed
16. Liu Z, Zhang C, Ding X, et al. A thermopile-based gas flow sensor with high sensitivity for noninvasive respiration monitoring. *Micromachines* 2023;14:910. DOI PubMed PMC
17. Al Farisi MS, Wang Y, Hasegawa Y, Matsushima M, Kawabe T, Shikida M. Facile in-tube-center packaging of flexible airflow rate microsensor for simultaneous respiration and heartbeats measurement. *IEEE Sens J* 2023;23:12626-33. DOI
18. Braun SR. Chapter 43 - Respiratory Rate and Pattern. In: Walker HK, Hall WD, Hurst JW, editors. *Clinical methods: the history, physical, and laboratory examinations*. Boston: Butterworths; 1990. Available from: <https://www.ncbi.nlm.nih.gov/books/NBK365/>. [Last accessed on 22 May 2024].
19. Gorini M, Misuri G, Corrado A, et al. Breathing pattern and carbon dioxide retention in severe chronic obstructive pulmonary disease. *Thorax* 1996;51:677-83. DOI PubMed PMC
20. Zulkifli NAB, Jeong W, Kim M, et al. Highly reliable magnetic-based pressure sensor utilizing simple microstructured PDMS: mechanical and design analysis via finite element analysis. *IEEE Sens J* 2021;21:16560-7. DOI
21. Pleil JD, Ariel Geer Wallace M, Davis MD, Matty CM. The physics of human breathing: flow, timing, volume, and pressure parameters for normal, on-demand, and ventilator respiration. *J Breath Res* 2021;15:042002. DOI PubMed PMC
22. Faghy MA, Brown PI, Davis NM, Mayes JP, Maden-Wilkinson TM. A flow resistive inspiratory muscle training mask worn during high-intensity interval training does not improve 5 km running time-trial performance. *Eur J Appl Physiol* 2021;121:183-91. DOI PubMed PMC
23. Krause-Sorio B, An E, Aguila AP, Martinez F, Aysola RS, Macey PM. Inspiratory muscle training for obstructive sleep apnea: protocol development and feasibility of home practice by sedentary adults. *Front Physiol* 2021;12:737493. DOI PubMed PMC
24. Langer D, Charususin N, Jácóme C, et al. Efficacy of a novel method for inspiratory muscle training in people with chronic obstructive pulmonary disease. *Phys Ther* 2015;95:1264-73. DOI PubMed
25. Kim TK, Kim JK, Jeong OC. Measurement of nonlinear mechanical properties of PDMS elastomer. *Microelectron Eng* 2011;88:1982-5. DOI
26. Wolf MP, Salieb-Beugelaar GB, Hunziker P. PDMS with designer functionalities - Properties, modifications strategies, and applications. *Prog Polym Sci* 2018;83:97-134. DOI
27. Lötvall J, Ekerljung L, Lundbäck B. Multi-symptom asthma is closely related to nasal blockage, rhinorrhea and symptoms of chronic rhinosinusitis-evidence from the West Sweden Asthma Study. *Respir Res* 2010;11:163. DOI PubMed PMC
28. Kim JS, Rubin BK. Nasal and sinus inflammation in chronic obstructive pulmonary disease. *COPD* 2007;4:163-6. DOI PubMed
29. Hung TQ, Kim DY, Rao BP, Kim C. Novel planar hall sensor for biomedical diagnosing lab-on-a-chip. In: Rinken T, editor. *State of the art in biosensors - general aspects*. 2013. DOI
30. Kim M, Oh S, Jeong W, et al. Highly bendable planar hall resistance sensor. *IEEE Magn Lett* 2020;11:1-5. DOI
31. Jeong W, Kim M, Ha JH, et al. Accurate, hysteresis-free temperature sensor for health monitoring using a magnetic sensor and pristine polymer. *RSC Adv* 2019;9:7885-9. DOI PubMed PMC
32. Yoo J, Lee YR, Kim H, Sul SK. Shielding technique for noise reduction in hall-effect current sensor of voltage source inverter. In: 2022 IEEE Energy Conversion Congress and Exposition (ECCE); 2022 Oct 09-13; Detroit, USA. IEEE; 2022. p. 1-5. DOI
33. Alhuthail E, Stockley J, Coney A, Cooper B. Measurement of breathing in patients with post-COVID-19 using structured light plethysmography (SLP). *BMJ Open Respir Res* 2021;8:e001070. DOI PubMed PMC
34. Koppurapu VS, Puliaiev M, Doerschug KC, Schmidt GA. Ventilated patients with COVID-19 show airflow obstruction. *J Intensive Care Med* 2021;36:696-703. DOI PubMed PMC
35. Ni X, Ouyang W, Jeong H, et al. Automated, multiparametric monitoring of respiratory biomarkers and vital signs in clinical and home settings for COVID-19 patients. *Proc Natl Acad Sci U S A* 2021;118:e2026610118. DOI PubMed PMC
36. Formiga MF, Roach KE, Vital I, et al. Reliability and validity of the test of incremental respiratory endurance measures of inspiratory muscle performance in COPD. *Int J Chron Obstruct Pulmon Dis* 2018;13:1569-76. DOI PubMed
37. McConnell AK, Romer LM. Respiratory muscle training in healthy humans: resolving the controversy. *Int J Sport Med* 2004;25:284-93. DOI PubMed